8-24-2011

Synthesis, Field Emission and Associated Degradation Mechanisms of Tapered ZnO Nanorods

Gregory M. Wrobel Mr.
gregory.wrobel@uconn.edu

Synthesis, Field Emission and Associated Degradation Mechanisms of Tapered ZnO Nanorods

Gregory Michael Wrobel

B.S., University of Connecticut, 2008

A Thesis

Submitted in Partial Fulfillment of the

Requirements for the Degree of

Master of Science

at the

University of Connecticut

2011

APPROVAL PAGE

Master of Science Thesis

Synthesis, Field Emission and Associated Degradation Mechanisms of Tapered ZnO Nanorods

Presented by

Gregory Michael Wrobel, B.S.

Major Advisor _____

Puxian Gao

Associate Advisor _____

Bryan Huey

Associate Advisor _____

George Rossetti

University of Connecticut

2011

Acknowledgements

Firstly, I would like to thank my family for their love and support. Without them I wouldn't have had the courage and opportunities that have made it possible to complete this thesis work.

Secondly, I would like to express my appreciation to all who have contributed toward the completion of this thesis. First, I want to thank Dr. Puxian Gao who has been my major advisor for the following work. Additionally, I would like to thank Drs. Sameh Dardona and Marcin Piech for being my industrial advisors who have both offered invaluable insight and resources for the project. Furthermore, I would like to thank Drs. Bryan Huey and George Rossetti for kindly serving as my associate advisors. Additional thanks go to Dr. Joseph Mantese for his support and the United Technologies Research Center for providing funding to this project and access to their facilities.

Finally, I am obliged to Paresh Shimpi, a PhD student at the University of Connecticut, and Dr. Yong Ding at Georgia Institute of Technology for his their excellent TEM work. Additional thanks go to Dr. Amra Peles from the UTRC for her DFT calculations.

TABLE OF CONTENTS

List of Tables

List of Figures

List of Equations

Synthesis, Field Emission and Associated Degradation Mechanisms of Tapered ZnO Nanorods

Gregory Michael Wrobel, M.S.

University of Connecticut, 2011

Modern development of field emitter arrays (FEA) has been made possible, partly thanks to the synthesis and development of one-dimensional (1D) nanostructures. High aspect ratio 1D nanostructures effectively amplify the electric field at the emitter tips, allowing electrons to be extracted at relatively low electric field. An inexpensive and rationally-controlled method to synthesize FEAs may permit commercial development of the field emission display (FED) technology, which can potentially outperform modern liquid crystal display (LCD) technology.

In this thesis work, we have developed a low-cost approach to produce large-scale ZnO nanorod FEAs, and systematically studied correlated degradation mechanisms including, exposure to gas species at high-voltage, and high-current emission.

Nanorods of ZnO were grown directly from iron and copper substrates by solution processing, without surface pre-treatment such as seed or catalyst layer. Field emission measurements show high current density and low turn-on voltage. Annealing under

vacuum effectively lowers turn-on voltage and enhances the maximum current density up to two orders of magnitude, as compared to initial field emission characteristics.

Two typical field emitter degradation mechanisms, including exposure to atmospheric gas species (O_2, N_2, and H_2) during field emission and high current induced degradation of the emitter tips, have been studied experimentally and theoretically. Experimental results suggest the presence of each gas species suppress the field emission current, which is supported by density functional theory (DFT) calculations. A tip-degradation phenomenon of ZnO nanorod FEAs has been observed during high-current field emission, which is most likely induced by a resistive joule heating process, which could result in a steady state temperature at the nanorod tip above the melting point of ZnO as suggested by calculation.

This thesis work provides insight to better help understand how these tapered ZnO nanorods perform as field emitters and determine if they're suitable for use as a commercial field emission source.

CHAPTER 1: INTRODUCTION

1.1 Field Emission Basics

1.1.1 Basic Description

The general definition of field emission (FE) can be defined as follows: when sufficiently high electric field is applied to the surface of a condensed phase of matter, typically a solid, electrons may gain adequate energy to tunnel through the surface, into vacuum[1]. Unlike thermionic emission or photoemission, where electrons with sufficient energy migrate *over* the potential surface barrier into vacuum, field emitted electrons tunnel *through* the surface potential barrier making FE a unique mode of electron emission. FE has undergone much theoretical and experimental investigation over the past century because of its promising potential for various electronics and optoelectronics applications[2].

1.1.2 Applications

The first major FE application breakthrough was the field emission source electron microscope, developed by Müller[3], which has helped push the limit of spatial resolution in modern electron microscopy to the atomic scale.

FE has provided valuable insights to physical and chemical adsorption phenomena, which directly impacts technological development of gaseous phase detection and catalytic reaction interpretation. Intrinsic field emission characteristics are altered by surface impurities. Careful assessment of these associated changes have been

used to enhance understanding of surface science. For instance, physical adsorption of inert gases on tungsten field emitters helped confirm the step-by-step surface contamination mechanism, by which multi-layer contamination proceeds only after completion of the first monolayer[4, 5]. Furthermore, field emission had been used to study contact-potential, surface mobility and other physical and chemical characteristics of chemisorbed surface species as well[1].

Presently, FE sources find home as industrial/research tools, mainly as electron sources used in vacuum electronics, i.e., ionization sources and microwave amplifiers[2]. There are currently no field emission based devices commercially available to the public.

An exciting modern application concept is the field emission display (FED). Working as a combination of the cathode ray tube and the modern LCD display, FEDs operate pixel-by-pixel[6]. Within each pixel is an array of field emitters pointed toward various phosphor compounds that emit photons when hit with electrons. Separate colors, i.e. red, blue and green, are generated with different phosphor compositions and the number of electrons per unit time dictates the relative brightness of each color[6]. With variations to the former, all colors can be simulated. Prototype FEDs have been built, but have yet to find their way into production. Limitations arise from the tradeoff between cost and quality of FE sources and degradation of field emitters, which has so far prevented commercially available products.

1.2 Field Emission: Historical Perspective

In 1897, R. W. Wood discovered what he called autoelectron emission[7], later renamed as field emission (FE). In 1919, J. Lilienfeld, had gotten a patent for his FE tube device[8], which operated by subjecting a pointed cathode to a large electric field within a high-vacuum x-ray tube, he was able to emit an electrical current of a few milliamps into vacuum[9].

Prior to Lilienfeld, Dushman, Langmuir and Hull had noted the FE effect in 1914, but their results weren't published until 1930[10]. Following the publication, Coolidge and Langmuir made further observations using a modified piece of tungsten wire[8]. During these early stages of experimental FE research, consistent experimental results had proven difficult to reproduce and consequently, experimental interest had declined.

Schottky made the first theoretical attempt to explain FE by expanding his thermionic electron emission theory by expanding the guidelines of the well established Schottky theory of thermionic emission in 1923[11]. He assumed FE followed the same emission mechanism as thermionic emission, with an added electric field factor to formulate the following:

$$i = AT^2 \exp\left(-\frac{\chi}{kT} + \frac{e^{\frac{2}{3}} F^{\frac{1}{2}}}{kT} \right)$$

Equation 1

Where χ is the material work function, e is electron charge and F is the applied electric field. The theory had been confirmed using thermionic emission at relatively low electric field[8]. This assumed only electrons with thermal energies greater than the work function, χ, can escape the metal surface, meaning FE should depend on temperature, with the rate limiting case as follows:

$$\frac{\chi}{kT} = \frac{e^{\frac{3}{2}} F^{\frac{1}{2}}}{kT}$$

Equation 2

As it turns out, the increase of current with temperature is less than the theory predicted and there's no consideration of cooling by loss of electrons, suggesting Schottky's theory of FE was incorrect[8].

In 1926, Milliken and Eyring discovered that current extracted from a sharp tipped tungsten wire was independent of temperature, suggesting that electrons extracted by FE were not the same as those extracted by thermionic emission[12]. They found it possible to accurately reproduce their results, by "current conditioning" (CC) the wire with high current prior to FE experiments. They proposed the effectiveness of CC resulted from smoothening of sub-micron asperities at the wire apex by ion bombardment.

They discovered electron emission was independent of temperature above 700°C, and the logarithm of current did not follow the linear trend as the Schottky equation had predicted[8].

During the same period of time, Gossling *et al.* preformed experiments using arrays of fine wires, and single electrochemically etched wires[13]. First they had noticed the effect CC and claimed the mechanism resulted from removal of surface sodium contamination. Following Schottky's theory, their measurements were plotted as logarithm of current verses the square-root of electrical potential between the anode and cathode. The plot didn't follow a straight line as predicted by the current theory. They carefully found that FE current was independent of temperature in the range of 573-1773°C and concluded that FE may be better described by quantum theory, rather than Schottky's classical theory[13].

In 1928 Millikan and Lauritsen discovered that the logarithm of current plotted against the reciprocal electric field yields a straight line, leading to the development of the equation that follows[14]:

$$i = A(T + cF)^2 \exp\left(-\frac{b}{T + cF}\right)$$

Equation 3

Where F is field strength and A, b, and c are constants. Equation 3 suggests that an increase of electric field is like increasing electron temperature within the metal. Despite the straight line produced by rearranging equation 3 to yield a plot of log(i) vs $1/F$, the theory falls short by neglecting quantum effects.

During the same period of time, other research groups like, Del Rosario[15], Piersol[16], and De Bruyne[17] had made observations suggesting field emission is

independent of temperature. Subsequently, Richardson[18] and Houston[19] had worked to improve upon the Schottky theory, still leaving room for improvement.

Fowler and Nordheim developed the first satisfactory field emission theory[20]. By combining results with Nordheim's theory for thermionic emission[21], they derived an emission formula containing effects strong electric fields and high temperature as follows:

$$I = \frac{\varepsilon}{2\pi h}\frac{\mu^{\frac{1}{2}}}{(\chi+\mu)\,\chi^{\frac{1}{2}}}F^2\exp\left(\frac{-4\kappa\chi^{\frac{3}{2}}}{3F}\right) = 6.2\cdot 10^{-6}\frac{\mu^{\frac{1}{2}}}{(\chi+\mu)\,\chi^{\frac{1}{2}}}F^2\exp\left(\frac{-2.1\cdot 10^{8}\chi^{\frac{3}{2}}}{F}\right)$$

Equation 4

Where I is current per cm^2 of emitting area, ε is electronic charge, h is Plank's constant, μ is the parameter for electron distribution in the Fermi-Dirac statistics equivalent of the thermodynamic potential of an electron, χ, is the work function of field emitter, $\kappa^2 = 8\pi^2 m/h^2$, and F is applied field. A simplified form of this expression is still used to describe field emission phenomena to this day.

1.3 Objective of Thesis

The objective of this thesis work is to cost-effectively synthesize tapered ZnO nanorods, on copper and iron electrode substrates using a solution processing technique. SEM analysis will show areal density of nanorods on each substrate and TEM analysis will confirm emitter structure, crystallinity and geometry.

Following, the intrinsic field emission performance of iron and copper-grown ZnO nanorods will be investigated. Turn-on and threshold electric field will be determined in addition to field enhancement factors.

Degradation mechanisms of field emitters, specific to emitter material and geometry include, effects brought on by exposure to gaseous species and resistive joule heating. These two mechanisms will be examined experimentally and theoretically in this work.

The ultimate goal of this study is first, to generate a simple/cost-effective field emission array, which may hopefully find its way into commercial application such as the field emission display. Secondly, this work will enhance the understanding of FE degradation mechanisms of tapered ZnO nanorods.

1.4 Structure of Thesis

This thesis is divided into 5 chapters. Chapter 2 contains a review of field emission with emphasis on theory and physical aspects of FE including emitter geometry, materials, synthesis and degradation mechanisms. Chapter 3 contains experimental procedures and materials used in this thesis work including chemicals, synthesis, characterization methods, and details of the field emission testing system. Chapter 4 contains the corresponding results and discussion, followed by conclusions and future studies in chapter 5.

CHAPTER 2: LITERATURE REVIEW

2.1 Field Emission: Principles

2.1.1 Emission from a Planar Surface

According to Fowler and Nordheim[20], the current density extracted from a planar metal surface under sufficiently large electric field obeys the following simplified equation:

$$I = \frac{\varepsilon}{2\pi h} \frac{\mu^{\frac{1}{2}}}{(\chi + \mu)\ \chi^{\frac{1}{2}}} F^2 \exp\left(\frac{-4\kappa\chi^{\frac{3}{2}}}{3F}\right)$$

Equation 5

Where I is current per cm^2, ε is electronic charge, h is Plank's constant, μ is the parameter for electron distribution in the Fermi-Dirac statistics equivalent of the thermodynamic potential of an electron, χ is the work function of field emitter, $\kappa^2 = 8\pi^2 m/h^2$, and F is applied field.

Therefore, to achieve a maximum current density at minimal electric field, an emitter with low χ and μ is desirable. Since field strength on the order of ~10^7 V/cm is required for electron tunneling to become probable from a planar source[20], it's impractical as a FE source. On the other hand, a high aspect ratio structure makes it possible to draw FE current at a much lower applied field.

2.1.2 Emission from Surface Irregularities

As it turns out, most surfaces generally contain a number of small surface irregularities including bumps and scratches…[11] Supplying an electric field in the presence of a surface irregularity causes electric field lines to accommodate the irregularity by "bending" around it resulting in a pile-up of field lines at the apex, as seen in *Figure 1*. This effect amplifies the electric field at the apex up to several orders of magnitude.

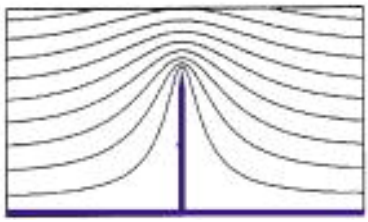

Figure 1: *Graphical representation of the electric field amplification mechanism in the presence of a high aspect ratio surface impurity[22]. The geometry of the impurity causes the electric field lines to bend and accommodate the non-planar geometry. The pile-up of electric field lines at the apex results in the local field amplification of up to several orders of magnitude.*

Accounting for the enhancement of electric field from surface irregularities, Stern, Gossling and Fowler reformulated the original Fowler-Nordheim equation to include a "field enhancement factor", β, as follows[23]:

$$\frac{d\log_e I}{dF_m^{-1}} = -2F_m - \frac{6.8\times10^7 \chi^{\frac{2}{3}}}{\beta}$$

Equation 6

Where F_m is the measured electric field, χ is the material work function and β is the field enhancement factor. Following the same line of thinking, the following formula was also developed, with A representing emission area:

$$\log_e A = 10.0 + \log_e I - \log_e \frac{\mu^{\frac{1}{2}}}{(\chi+\mu)\chi^{\frac{1}{2}}} - 2\log_e(\beta F_m) - \frac{1}{F_m}\frac{d\log_e I}{dF_m^{-1}}$$

Equation 7

With modern material processing techniques, it's rather easy to deliberately create high aspect ratio micro/nanorod features on the surface of a cathode with β ranging from 100-1000+. Factors influencing β include emitter aspect ratio, tip radii, orthogonal alignment relative to the substrate, and the distance between cathode and anode[22]. Since β depends on the distance between the cathode and anode, it doesn't explicitly describe the "quality" of the emitter(s). Single emitters can produce currents within the microamp range, but some applications require current densities greater than a single emitter can produce.

2.1.3 Field Emission Arrays

Field emission arrays (FEAs) prove useful when it's necessary to achieve current densities greater than a single emitter can produce. The maximum achievable current density from a FEA is rarely equal to the sum of current densities that would be extracted from lone emitter. When multiple emitters are in close proximity (within a few emitter lengths apart), the local amplification of electric field at the emitter apex is diminished when compared to a lone emitter. This effect is known as the screening effect. The local

field experienced by an emitter in this situation can be described with the following equation[24]:

$$F = s\frac{V}{r_0} + (1-s)\frac{V}{d} = \beta\frac{V}{d} \equiv \beta F_0$$

Equation 8

Where s is the screening factor, ranging between 0 for a single high aspect ratio emitter and 1 for a planar emitter, V is the applied voltage, d is the distance of separation between cathode and anode, β is the field enhancement factor and F_0 is the applied electric field. As the distance between emitters decreases, s gets closer to 1 and the field enhancement decreases.

There's a tradeoff between high β, which increases with emitter spacing, and emission current density, which increases with the number of emission sites[25]. Assuming that all emitters are identical, when packed too close together the FE source will simulate a planar emitter, requiring undesirably high field strength to attain desirable current density. When packed too sparsely, the current density will suffer. *Figure 2* graphically depicts the decrease of β as emitter spacing decreases. To achieve maximum current density from the FEA, Nilsson *et al.* have determined the ideal separation between emitters is approximately twice the emitter height by using Poisson's equation and assuming optimized geometry[22].

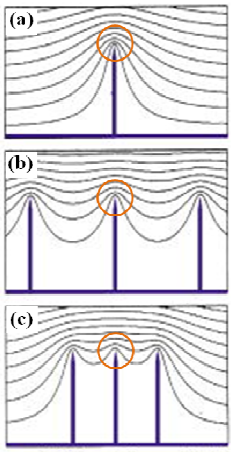

Figure 2: *Graphical depiction of electric field line pile-up in the presence of high aspect-ratio field emitter(s) as seen within each orange circle for: (a) single emitter; (b) spaced approximately equal to height; (c) spaced approximately ½ emitter height. Electric field line pile-up at the emitter tip apex is lessened as emitter spacing is decreased, which is a result of the screening effect. Figure courtesy of Nillson et al.*[22].

Factors for optimal field enhancement of FEAs includes, dimensional uniformity, tip-radius, alignment, spacing and distance from the anode[22, 24]. Within an array of non-uniform emitters, only the tallest emitters with the highest β contribute to FE because the electric field may not penetrate deep enough to reach shorter emitters as a result of the screening effect.

2.1.4 Semiconductor Emitters

The field emission theories discussed above are based on the assumption that the emission sources are made from metals, not semiconductors. If electrons within a semiconductor are to contribute to FE, they must first attain adequate energy to be excited over the band gap, into the conduction band[26]. Temperature is one source of this energy.

The presence of impurity atoms on or within a semiconductor influences electrical properties. For example, if an impurity atom within the semiconductor has a valence state different than the semiconductor, the system may be provided with additional electrons or holes, which can increase electrical conductance. This mechanism, is deliberately used in industry to modify electrical properties of semiconductors and is critical for today's modern electronic devices and is known as doping. Adsorbates on a semiconductor surface can also influence conductance[26].

Because of sensitivity to temperature and impurities, semiconductor field emission can be described differently than a metal. Under the unrealistic assumption that the applied field doesn't penetrate the semiconductor surface, emission current of a semiconductor can be represent by[1]:

$$i = \frac{2nekT}{(\pi m\phi)^{\frac{1}{2}}} \exp\left(\frac{-6.8 \cdot 10^{7}\phi^{\frac{3}{2}}}{F}\right)$$

Equation 9

Where n corresponds to the number of electrons per cm^3 within the conduction band, ϕ is the width of the conduction band and T is temperature[1]. Despite availability of this equation, the Fowler-Nordheim formula remains the primary theory used to describe FE from semiconductors because of its simplicity.

2.2 Material Selection

2.2.1 Introduction

As mentioned, FE source quality is dictated by both geometry and material properties. This section will briefly discuss materials commonly used as field emission sources.

2.2.2 Metals

Metals were the material of choice in early field emission studies, with tungsten dominating the field as a result of high melting temperature and its common use in thermionic emission and high temperature devices. Fabrication of metal emitters has been well refined but applications are limited to industry and research laboratories where high vacuum is available to limit oxidation.

2.2.2.1 Tungsten

Given the high work function of tungsten, 4.50-4.56eV, and the potential for oxidation at high temperature, modern tungsten FE applications are limited mainly to field emission microscope applications[27]. Tungsten emitters are typically single crystal wires with a tip radius of approximately ≤100nm and operated in high-ultrahigh vacuum to limit contamination/oxidation and extend emitter lifetime[1].

2.2.2.2 Molybdenum

Molybdenum has offered valuable insights to FE research, resulting from research on highly reproducible cone arrays. Molybdenum isn't ideal for application because it

can't be heated to sufficiently high temperatures to completely remove adsorbed species, without damaging the emitter(s)[28]. Current FE research generally focuses on materials with work function lower than Mo (~4.4eV) for decreased operating voltage[29].

2.2.3 Semiconductors

Field emission from semiconductors has proven to be complex because of intrinsic electronic properties. For example, surface work function (electron affinity), conductivity, etc., can be greatly altered in the presence of active gas species and there exists a strong dependence between temperature and electrical resistance[26]. Despite these complexities, semiconductors are heavily studied as FE sources, likely a result of popular bottom-up synthesis techniques capable of producing high-aspect ratio FEAs. Therefore, it's worth explicitly considering some promising semiconductor materials as field emitters.

2.2.3.1 ZnO

Although ZnO doesn't have the ideal material properties for field emission, ϕ ~5.2eV, T_{melt} = 1975°C, ZnO nanorod/wire arrays can be synthesized quickly (within 4hrs) at low cost and high yield on practically any substrate. Because of this ease of preparation, the possibility of quality inexpensive ZnO FEAs is a reality.

ZnO's electronic properties improve by two mechanisms. First, being an intrinsic semiconductor, ZnO undergoes an increase in conductivity as temperature increases, which is common during field emission[26]. Secondly, oxygen vacancies are generated on

the surface, leaving unpaired electrons to contribute to ZnO's intrinsic n-type conductivity[30].

2.2.3.2 GaN & AlN

GaN and AlN exhibit very high mechanical hardness and chemical inertness making these materials capable of withstanding moderate ion bombardment and resistant to degradation from elemental gas species.

The sp^3 type bonding of GaN and AlN's wurtzite crystal structure has four fold coordination, giving rise to a low or negative electron affinity (work function)[31]. GaN has an electron affinity of about 2.7-3.3eV[31]. Experimental evidence suggests that AlN may have a negative electron affinity, meaning conduction band electrons can be freely emitted into vacuum without an applied electrical potential[31, 32].

On the downside, GaN/AlN field emission arrays will often require expensive, electrically insulating substrates and gallium is known to be toxic and is expensive[25].

2.2.4 Carbon Based Materials

2.2.4.1 Diamond

Diamond has attracted much interest as an FE source because of negative electron affinity and extremely high hardness which resists ion bombardment[33]. It's been said that diamond's negative electron affinity may eliminate the need for fabricating sharp tipped emitters for adequate field enhancement, which are often complicated and costly to produce[34].

Since pure diamond is electrically insulating, doping is needed to increase conductivity if it's to be used as a FE source. Difficulties with doping have limited the success of diamond as a field emission source[35].

2.2.4.2 Carbon Nanotubes

Carbon nanotubes (CNT) are regarded by many as one of the most promising modern field emitter materials because of properties such as metallic conductivity, high aspect ratio and nanometer-scale tip radii. Typical tip diameters range from ~0.4nm to >3nm for single-walled CNTs. Unfortunately there is a substantial trade-off between the quality of CNT arrays verses the cost[36].

CNTs oxidize in the presence of oxygen and high temperature, which can be up to 2000K during FE[37]. High vacuum is needed to limit oxidation and may not be practical depending on application[38]. There's often high interfacial resistance between CNTs and the substrate, which may lead to high interface temperatures and detachment of the CNT from the substrate. *Figure 3* shows a high quality CNT field emission array.

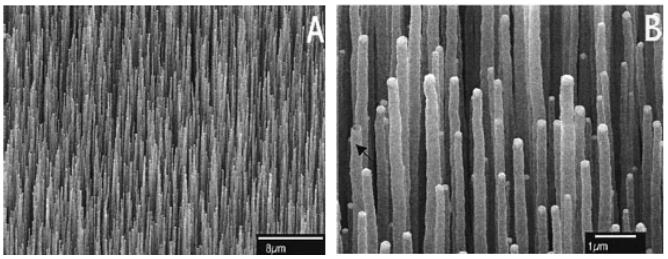

Figure 3: *A carbon nanotube array synthesized by a chemical vapor deposition method. Figure courtesy of Ren et al.*[39].

2.3 Material Processing

There are a variety of techniques to create the desired geometries of a particular material, each with its own tradeoff between uniformity and cost. This section will discuss some of the most common methods of creating field emitters.

2.3.1 Etching

Due to simplicity and consistency, metallic field emitters are often created by electrochemical etching techniques. As an example, the tip of a fine tungsten wire can introduced to an electrochemical etching solution, either sodium or potassium hydroxide, to produce a extremely fine tip, as small as 10nm[40], as seen in *Figure 4*.

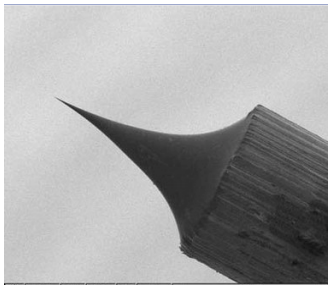

Figure 4: *SEM image of a tungsten wire with an electrochemically etched, ~10nm nanometer tip. Photo courtesy of University of Michigan*[40].

2.3.2 Vapor Deposition Methods

There are two main vapor deposition methods, physical vapor deposition (PVD) and chemical vapor deposition (CVD), both can be used in the creation of field emitters. Common PVD processes include, but are not limited to, sputtering, thermal evaporation, cathodic arc discharge and pulse laser deposition. PVD is often used to create the seeds needed to grow high aspect ratio structures by CVD or solution processing methods.

Common CVD systems operate as follows: A source material is vaporized at high temperature, is transported to a substrate of lower temperature, resulting in decomposition, reduction or condensation of the vapor species produces the desired material/structure[41].

Both methods are capable of producing high quality FEAs because of advantages including epitaxial alignment on substrates, uniform dimensionality and good crystallinity. Disadvantages may include high temperature synthesis, high cost, small-scale production and use of a specific substrate.

2.3.3 Hydrothermal/Solvothermal Synthesis

Hydrothermal/solvothermal solution processing techniques are widely used to synthesize functional materials, including field emitters, via chemical solution at elevated temperature and pressure[42]. Typically a substrate sits within chemical solution which is heated in an oven or furnace at ≥50°C for a series of hours.

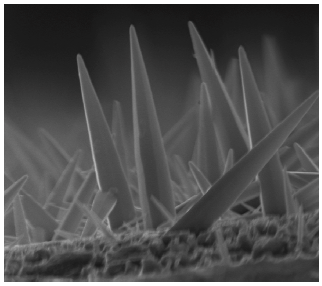

Figure 5: *A side view SEM image of ZnO nanorods synthesized on pure iron substrate using a hydrothermal synthesis method.*

Advantages of these techniques include low-temperature processing, low-cost, a wide range of structural dimensionality, large scale production and utilization of a wide

variety of substrates. Typical disadvantages include non-epitaxial alignment with the substrate, non-uniform areal density and dimensionality, crystal defects and poor substrate adhesion[42]. A side view image of ZnO nanorods synthesized using the hydrothermal method can be seen in *Figure 5.*

2.3.4 Lithography

Lithography is a top-down processing technique where material is selectively removed to make a desired pattern. A pattern is transferred from a template, know as a "mask", to a substrate[43] where it's processed into a physical structure as illustrated in *Figure 6*.

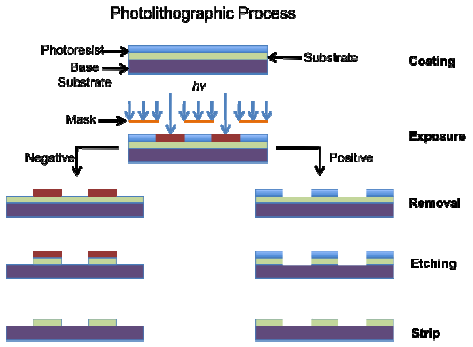

Figure 6: *A step-by-step schematic of photolithographic process. First, the substrate is coated with a layer of photoresist. Second, a mask is placed over the substrate/photoresist, leaving the un-masked region exposed to either UV light, an electron-beam or x-rays. Next, the un-masked photoresist is removed either in positive or negative (inverse) pattern, leaving the substrate to be preferentially etched in areas where the photoresist had been removed. Finally, the remainder of the photoresist is stripped away, leaving the desired pattern on the substrate.*

Lithography is a well-controlled process, capable of creating nearly perfect arrays of field emitters, like the uniform array of Ge emitters in *Figure 7*. The process requires

very expensive equipment and may require relatively time-consuming fabrication process limiting appication.

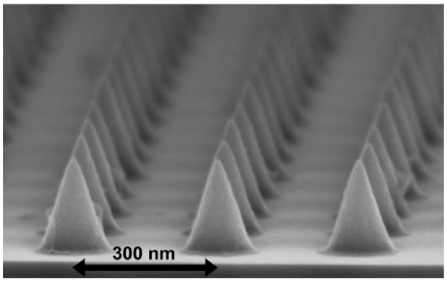

Figure 7: *A uniform array of nano-scale Ge field emitters created using photolithography. Cone dimensions are 130nm at the base, spaced 300nm apart. SEM image courtesy of Kontio et al.*[44].

2.4 Degradation Mechanisms

Degradation of field emitters remains as one of the foremost factors preventing widespread commercial use of field emission display technology. Common FE degradation mechanisms will be discussed in this section.

2.4.1 Resistive Heating

When subjected to high current density, electrical resistance heats and even melt/sublimate emitters if supplied with sufficiently large current density[45, 46].

Other than emission current, the maximum temperature, T_{max}, along the axis of an emitter depends on geometry. For example, when an electron at temperature T is emitted from a cylindrical emitter, it takes energy with it equal to about $(3/2)k_BT$, resulting in a cooling effect at the tip[47]. As a result, the maximum temperature is achieved below the

emitter apex (x < L), as seen in *Figure 8*(a), where *L* is emitter length and *x* is the relative distance along the emitter axis.

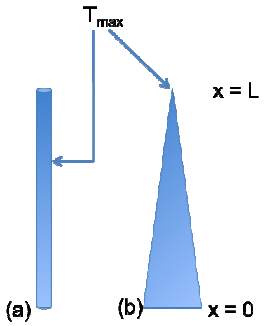

Figure 8: *Visual representation of maximum temperature (T_{max}) for: (a) cylindrical field emitter. (b) Conical field emitter.*

Unlike a cylindrical emitter, the maximum temperature of conical emitters occurs at the emitter apex where x = L, as seen in *Figure 8*(b). The tip cooling effect is negligible compared with the heat generated at the apex, which has the smallest cross sectional area and therefore the highest current density along the emitter[48]. Materials with high electrical conductivity are less likely to heat up to a critical temperature.

A generalized equation can be used to estimate the T_{max} of both emitter geometries[48] and is discussed in chapter 4.

2.4.1.1 Interfacial Degradation

There exists an interface between every field emitter and substrate. Some interfaces may be laden with defects, producing high electrical resistance and poor adhesion. This is often the case when there is a lattice mismatch between emitter and substrate. With sufficiently large FE current, field emitters may detach from the substrate either by heating, the attraction between anode and cathode or a combination of the two.

It's best to use a clean substrate with lattice spacing similar to the emitter material to reduce interfacial defects.

2.4.2 Exposure to Gaseous Species

2.4.2.1 Ion Bombardment

Ion bombardment is said to be the major factor limiting the long operating life of field emitters[49]. As electrons travel from the anode to the cathode, some will ionize gas molecules, creating positively charged ions which are accelerated toward the negatively charged emitters, causing damage by sputtering. Even within high vacuum, there remains a sufficient quantity of gaseous species to cause damage. Ultrahigh vacuum and materials with a high hardness help to mitigate the problem.

2.4.2.2 Surface Contamination

As previously discussed, electronic properties of some semiconductors are greatly affected by the presence of particular gas species in the surrounding atmosphere. For example, when exposed to oxygen, electrons in SnO's conduction band are adsorbed on the material surface, resulting is space-charge layer which alters the surface conductivity[50].

If the quality of field emission is dependent on the vacuum induced electrical properties, it's important to maintain the desired ambient. This remains a limitation for commercial application where vacuum ambient is difficult to maintain without vacuum equipment.

2.4.3 Summary

With so many different materials and geometries to make field emitters and substrates, there's no one set of parameters to follow that will yield a long lasting emission source. Careful consideration of materials and associated degradation mechanisms are needed to assess the limitations of the system and minimize degradation.

CHAPTER 3: EXPERIMENTAL PROCEDURES

In this section, the experimental procedures used in this thesis research has been summarized, including nanorod-based field emitter synthesis, structural/chemical characterization, and field emission setup/measurement.

3.1 Synthesis of Field Emitters

Rods, 1.27cm in diameter, of iron (99.95%, Goodfellow), and copper (99.99%, Alfa Aesar) were used to make substrates. The rods were machined into 1.59cm long blanks, with a 0.5cm wide × 0.4mm tall "FE-platform" in the center, as seen in *Figure 9*. The top FE-platform surface was processed by standard metallurgical grind and polish procedure, ending with a 6μm diamond polish. Substrates were cleaned by sonication in hexanes for 3min followed by plasma cleaning in argon gas for 2min.

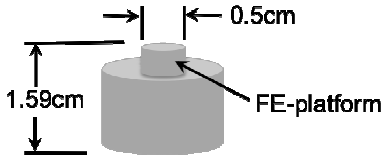

Figure 9: *Schematic of the ZnO field emission substrate. The field emitters are synthesized on top of the polished FE-platform.*

Synthesis of tapered ZnO nanorod field emitters was executed using a solution-processing method. A 100mL PTFE container, depicted in *Figure 10*, was filled with 88mL aqueous solution containing 20mM of both zinc nitrate hexahydrate ($Zn(NO_3)_2.6H_2O$, ZNH) and hexamethylenetetramine ($C_6H_{12}N_4$, HMT). An addition of 140mM of 1,3-diaminopropane (DAP) was added as a growth modifier, promoting the

tapered shape of the nanorods. Substrates were suspended up-side down in the solution to prevent any ZnO precipitates from settling on the substrate surface. Synthesis was performed at 60°C for a period of 18 hours. Samples were then rinsed with de-ionized water and dried in air.

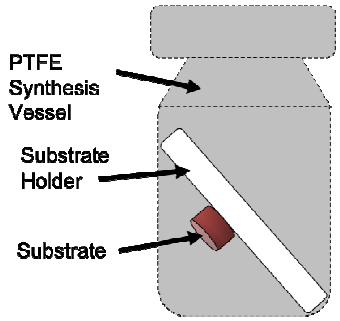

Figure 10: *Schematic of vessel used to synthesize tapered ZnO nanorods. The metal substrate is suspended up-side down on a PTFE sample holder to prevent ZnO precipitates from settling on the top surface.*

3.2 Post-Synthesis Analysis

An ultraviolet-visible spectrometer (UVS; Agilent Cary 5000) was used to study substrate cation concentrations as a function of time. To visualize changes of substrate surface roughness by etching, 2.5cm x 0.2cm substrates of copper and iron were polished to 250nm and subjected to 18hr treatment in a solution of 20mM HMT and 140mM DAP. Following, samples were analyzed using JEOL 6335F field emission scanning electron microscope (FESEM).

3.3 Field Emission System

All field emission studies were preformed within a vacuum chamber at a base pressure of 5×10^{-8} torr. A special heater sleeve was designed to accommodate the substrate, spacer and anode as seen in *Figure 11*. The gap between cathode and anode

was established using an insulating ceramic spacer. A gap of 120μm was maintained when measuring intrinsic copper and iron-grown ZnO FE properties and a gap 60μm was established for all gas effect studies.

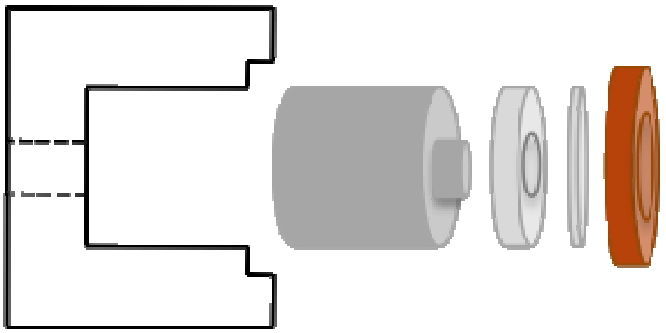

Figure 11: *Schematic of the field emission assembly. From left to right: heater sleeve, substrate, ceramic spacer, anode and power supply, respectively. The* (+) *power supply is in direct electrical contact with the anode and holds the components in place with screws. The electrical ground enters through the back of the heater sleeve and screws into the back of the substrate, which is threaded.*

Voltage was supplied to Fe samples with a Keithley 240 series high voltage source and field emission current was measured with a Keithley 6485 Picoammeter connected in series with a 10 MΩ resistor between cathode (substrate) and anode. For all experiments, voltage was ramped in 10V increments with a 2 second dwell.

All FE samples were current conditioned improve nanorod field emission characteristics and repeatability. FE samples were held at a constant 12.5 V/μm until current reached a maximum.

3.4 Structural and Chemical Characterizations of Field Emitters

ZnO nanorod composition, morphology and structure were characterized using a JEOL 6335F field emission scanning electron microscope (FESEM) attached with an

energy dispersive x-ray spectrometer (EDXS), a Physical Electronics Model 670 Auger Electron Spectrometer (AES), and a FEI Tecnai T12 transmission electron microscope (TEM).

Sputter assisted Auger analysis was performed in a Physical Electronics Model 670 Auger Electron Spectrometer (AES) to investigate the presence of surface contamination and the possibility of substrate induced nanorod doping. Samples created for Auger analysis were not used as field emission sources.

TEM samples were made by pressing a carbon coated TEM grid on the nanorod covered surface, causing nanorods detach from the substrate and stick to the TEM grid, which were then ready for TEM imaging and diffraction analysis.

3.5 Degradation Studies

3.5.1 Studying Effects of Gas Exposure

Prior to gas exposure experiments, a base pressure of $5x10^{-8}$ torr was established within the vacuum chamber. Single gas species (H_2, N_2, or O_2, Matheson Gas, 99.999%) were introduced into the chamber until the pressure reached 5.0×10^{-5} torr. High voltage of 850V (14.17 V/μm) was supplied to the nanorods for 1000 seconds while holding constant vacuum pressure. The voltage was then removed and the system was returned to 5×10^{8} torr. Alterations from original emission characteristics were studied by ramping voltage up to 1100V in 10V steps. Next, the samples were heated in vacuum at 450°C for

30min to remove surface bound gas and then ramped to 1100V to study any alterations in FE performance. Separate samples were used for each gas exposure experiment.

First-principle studies were carried out by Dr. Amra Peles at the United Technologies Research Center (East Hartford, CT). Calculations were based on spin polarized density functional theory (DFT)[51, 52] using generalized gradient approximation (GGA)[53] and projector augmented wave (PAW) method as implemented in the VASP code[54-56]. The cut-off energy for a plane wave basis set was 400eV and the Brillouin zone was sampled using a Monkhorst-Pack sampling technique[57] with 8×8×4 and 12×12×1 k-point grid for bulk and surface calculations, respectively. Surfaces were modeled as a 1×1 (0001) periodic slab with eight ZnO layers separated by 32Å vacuum layer. A dipolar correction was introduced in a direction perpendicular to the (0001) surface to take into account polarity of surface.

3.5.2 Studying the Effects of High Current

To study high current induced degradation, ZnO was synthesized on commercially available tungsten wire. A fine tip was produced by electrochemical etching in KOH solution. Following, wires were cleaned by sonication in hexanes for 3min. ZnO synthesis was carried out using the same solution processing method mentioned in section 3.1 without the polishing step.

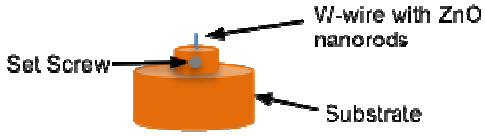

Figure 12: *Schematic of substrate used for testing of ZnO nanorods on a fine tungsten wire. The wire was mounted in a machined hole and held in place with a set-screw. The gap between cathode and anode is unknown.*

The wire was mounted on a bare copper substrate with a hole and set-screw, as seen in *Figure 12*. The gap between the cathode (wire) and anode was unknown and therefore electric field cannot be determined. Voltage was ramped to 250V to establish a baseline, followed by voltage scans from 0-250V, 0-300V and 0-350V, respectively to induced permanent degradation of the field emitters. SEM images of the sample were taken before and after to observe the nanorod morphology changes.

CHAPTER 4: EXPERIMENTAL RESULTS & DISCUSSION

4.1 Introduction

There are two main goals of this study. First is to outline the intrinsic field emission performance of copper and iron-grown ZnO nanorods synthesized using the described solution processing technique, which includes turn-on electric field (when J = 0.1μA/cm^2), and threshold electric field (when J = 1mA/cm^2), and field enhancement factor, β, will be resolved.

Secondly, investigation of the degradation mechanisms associated specifically with tapered ZnO nanorods, including exposure to the major gas species found in air and degradation due to high current field emission. The goal is to improve scientific understanding of the mechanisms responsible for degradation of tapered ZnO nanorod field emitters.

4.2 SEM and TEM results

Figure 13 illustrates typical ZnO nanorods synthesized on copper and iron substrates. A FESEM image of ZnO grown from copper is illustrated in *Figure 13*(a), which shows closely packed arrays of ~11.5μm long rods characterized by ~10-25nm tip diameter and an average areal density of ~3.7×10^5 mm^{-2}. Similar morphology was attained previously with nanoparticle seeded glass and silicon surfaces[58, 59].

In contrast, ZnO nanorods grown on iron surfaces, shown in *Figure 13*(b), are characterized by longer, ~14 μm, nanorods with tip diameters of 8-30nm, with a measured areal density of ~5.0×10^3 mm^{-2}, significantly less than that of copper. ZnO rods grown directly on glass surfaces exhibited similar morphology[60]. The characteristic ZnO nanorod morphology data can be found in *Table 1*.

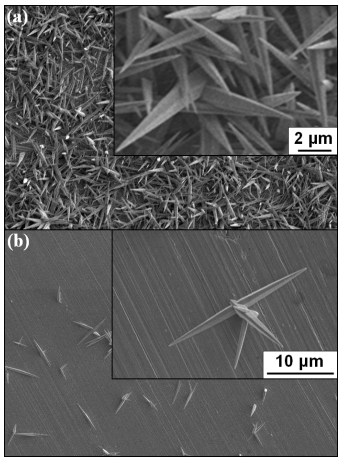

Figure 13: *SEM micrographs of ZnO nanorods characteristic of 6μm polished metal electrode substrates: (a) Copper: (b) Iron:*

ZnO Nanorod Film Morphology		
	Iron	**Copper**
Areal Density (mm^{-2})	5 x 10^3	4 x 10^5
Avg. Rod Length (μm)	14	11.5
Avg. Tip Diameter (nm)	8-30	10-25

Table 1: *Dimensionality and spatial characteristics of ZnO nanorods grown from iron and copper substrates.*

Even though ZnO nanorods arrays have been synthesized with similar morphology in earlier reports[58-60], the techniques generally require a seeding step prior to synthesis. The seeding step adds time and cost to the synthesis process and it would be of benefit to skip it if suitable morphology can be achieved.

Transmission electron microscopy (TEM) imaging, *figure 14(a),* has revealed that the ZnO nanorods are single crystalline, as depicted by the diffraction pattern as seen in *Figure 14(b)*. The diffraction pattern indicates the nanorods grow in the $[1\bar{1}21]$ direction.

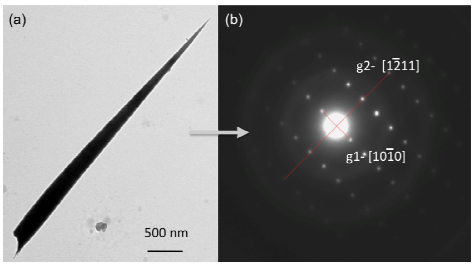

Figure 14: *(a) TEM image of a typical ZnO nanorod grown from the iron substrate. (b) Corresponding diffraction pattern showing the nanorod is single crystalline with growth in the [*$1\bar{1}21$*] direction.*

4.3 The Synthesis Solution

The tapering of the nanorods has been explained by reversible DAP adsorption on the ZnO (0001) facet during synthesis. This slows Ostwald ripening and preserves minute (0001) steps resulting in the tapered shape[58], like those seen in *Figure 13 & 14*.

It's well known that structures synthesized via low temperature solution processing can be laden with crystal defects and surface adsorbates, which can hinder field emission performance. The negative effect is manifested within choppy field emission hysteresis loop formed between *J vs. E* generated by forward and reverse voltage sweeps of the as-grown samples, as shown in *Figure 15*.

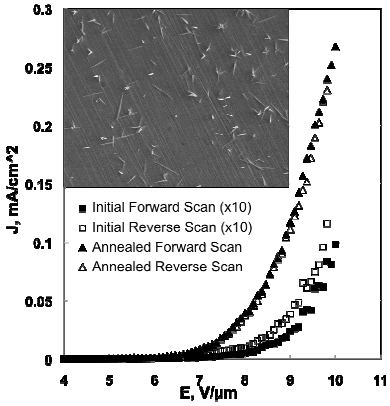

Figure 15: *The J-E characteristics of ZnO nanorods before and after current conditioning. Note: the intital scans have been multipied by 10X to better show hysteresis. Inset: an SEM image of iron-grown nanorods.*

Ultraviolet-visible spectroscopy (UVS), revealed the presence of dissolved copper or iron cation species in addition to zinc species within the growth solution. The resulting calculated etch rate of the iron substrate was below the sensitivity limits of the UVS technique (<1nm/h), further supported by lack of visual etching in *Figure 13(b)*.

There was a steady increase in Cu^{2+} cation concentration throughout the duration of the synthesis process, shown in *Figure 16*, which corresponds to the gradual dissolution of the Cu substrate. Deduced from the data in *Figure 16*, there's a significant change in the substrate dissolution rate from ~50nm/h to ~20nm/h, nearly 3h after the reaction start. This change may be related to the amount of time needed to dissolve the surface oxide layer before the ZnO nucleation and growth are initiated. Interestingly, the sputter assisted Auger Electron Spectroscopy (AES) analysis showed no evidence of Cu doping within the ZnO nanorods. This is likely due to a much lower Cu^{2+} concentration (~0.2mM) compared to the Zn^{2+} (~20mM) and possibly a markedly stronger chelation of the Cu^{2+} cations by the DAP ligands as compared to Zn^{2+}.

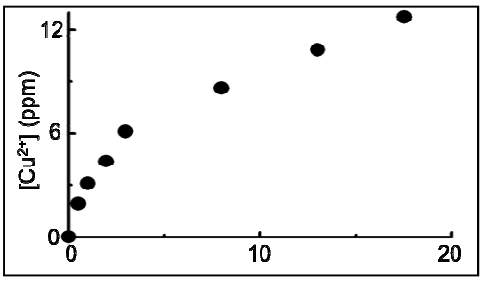

Figure 16: *Cu^{2+}*concentration in the synthesis solution as a function of time. *Initially the etch rate is estimated at ~50 nm/hr, reducing to about ~20 nm/hr after approximately 3hrs after the start of synthesis reaction.*

Morphological changes of the substrate surface as a result of synthesis-solution induced chemical etching can be seen in *Figure 17*. These samples were subjected to 18hr in a solution containing 20mM HMT and 140mM DAP without ZNH. From *Figure 17* (a) & (b) it's evident that copper substrates undergo drastic morphology changes, unlike iron (c) & (d), which had etched little to none.

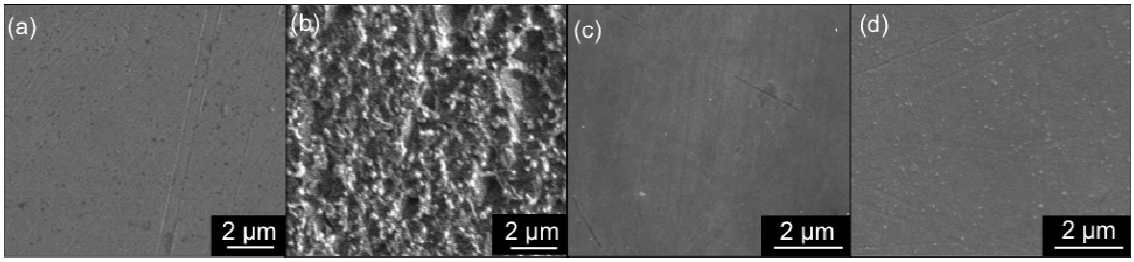

Figure 17: *SEM micrograph showing surface etching of copper (a, b) and iron (c, d) substrates after 18hr in a solution containing 20mM of HMT and 140mM DAP. Copper undergoes substantial morphology alteration while the effect on iron is minimal.*

4.4 Auger Analysis

Interestingly, sputter-assisted Auger analysis spectra of synthesized ZnO nanorods revealed the absence of both iron or copper doping, despite the presence of these cations within the growth solution, as shown in *figure 18*. This suggests a much stronger chelation of these cations by DAP as compared to Zn^{2+}.

The Auger spectra reveals the presence of a substantial amount of surface impurities on the "as-synthesized" ZnO nanorods on both substrates, as seen in *Figure 18*(a) and (b) respectively. About 15% of detectable species on copper-grown nanorods are carbon/nitrogen while the iron-grown nanorod surface shows 38% carbon.

To better understand internal chemical composition, about 2000Å of material was sputtered away from the nanorod surface. The Auger spectra shows the carbon and nitrogen peaks disappear, proving these impurities were only present on the surface and may likely be the cause of hysteresis in the field emission performance prior to CC.

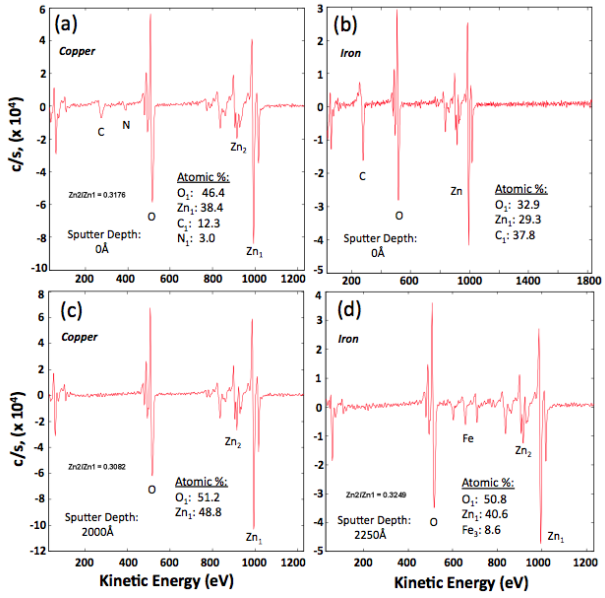

Figure 18: *Sputter assisted Auger analysis spectra of ZnO nanorods synthesized on copper (a) before sputtering and (c) after 2000Å of sputtering: iron substrate (b) before sputtering and (d) 2250Å sputtering depth. Note: (d) shows iron signal, which is a confirmed artifact from iron deposited onto the ZnO nanorod surface as an outcome of the sputtering step.*

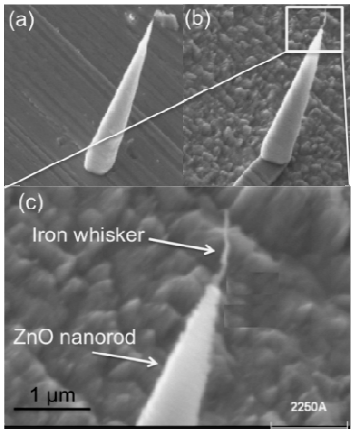

Figure 19: *SEM image of a ZnO nanorod (a) before sputtering, (b) after sputtering where an iron whisker had been deposited at the apex as a result. (c) magnified view of the iron whisker. The iron whisker in (b), (c) wasn't present before sputtering.*

An interesting artifact had shown up in the Auger spectrum in *Figure 18*(d), which shows an iron signal. At first glace, the data seems to indicate iron doping within the nanorods. It's not without the insight shown in the SEM micrograph in *Figure 19*, which shows an iron-grown nanorod before and after sputtering, respectively, suggesting the signal was an artifact of sputtering. With the large amount of iron exposed to sputtering, an iron whisker had been deposited on the tip and body of the nanorod (*Figure 19*(c)). For further investigation, iron-grown nanorods were deposited onto a silicon substrate for further analysis. In this case, Auger analysis didn't detect any iron within the nanorods, proving the iron signal in *Figure 18*(c) was an artifact of sputtering. Therefore, the iron signal in *Figure 18* and the whisker in *Figure 19* had formed during sputtering, not during synthesis.

4.5 Field Emission Characteristics

The measured current density as a function of applied field (*J-E* curve) from copper and iron-grown nanorods are shown in *Figure 20*(a) and *Figure 20*(b) respectively. Each *J-E* plot, contains a curve acquired before and after current conditioning (CC) represented by (×)'s and (•)'s respectively. A current vs time plot obtained from CC can be seen in ***Figure 21***. CC was halted when the current reached a maximum.

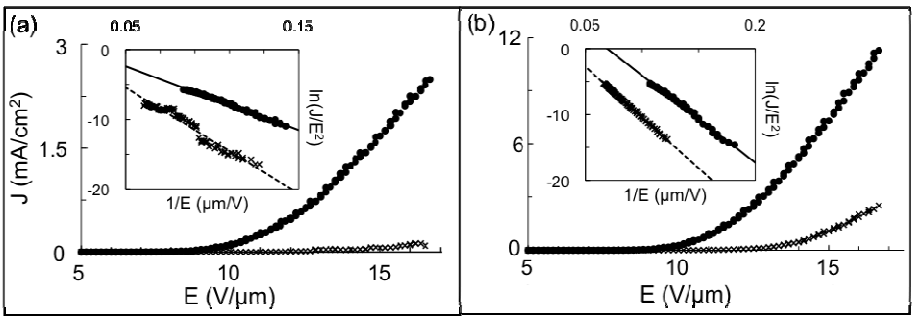

Figure 20: *Measured field emission current density as a function of electric field before (symbol: ×) and after (symbol: •) current conditioning for ZnO nanorods on (a) copper, (b) iron. Insets are the corresponding F-N plots from which β is calculated.*

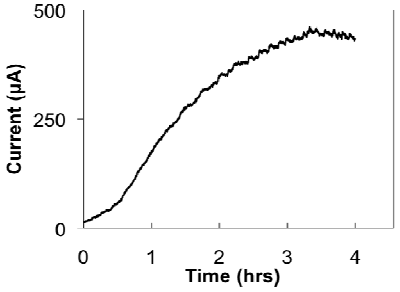

Figure 21: *An example plot of a current conditioning current vs. time plot taken from an iron field emission sample. The sample was held at a constant electric field of 12.5V/μm until current reached a plateau. At the start, current was about 13μA and had increased to about 450μA after ~4hrs of conditioning.*

In general, the field emission current density is described by the Fowler-Nordheim (F-N) equation:

$$J = A(\beta E)^2 \exp\left(-B\frac{\phi^{\frac{3}{2}}}{\beta E}\right)$$

Equation 10

where J is the current density, E is the electric field strength, β is the electric field enhancement factor, Φ is the material work function, and A and B are constants[20].

A value of β can be obtained by rearranging the to the F-N equation to form a linear trend (*Figure 20* insets) with a slope equal to $-\left(\frac{B\phi^{3/2}}{\beta}\right)$. Using literature reported values of 6.83×10^9 V eV$^{-3/2}$ m^{-1} for B and 5.56 eV for Φ, β was resolved for these samples and is summarized in *Table 2*

It's clear from the plots in *Figure 20* that CC improved nanorod field emission characteristics. The measured turn-on field for copper-based samples decreased from 8.94V/μm to 6.17V/μm, and threshold field decreased from a value exceeding 17V/μm to 13.5V/μm and β increased from 853 to 1010. Turn-on field for iron-grown samples decreased from 8.05V/μm to 6.5V/μm, threshold field changed from 14.6V/μm to 10.9V/μm and β increased from 572 to 676. The results are summarized in *Table 2*.

Comparison of *Figure 20*(a) and *Figure 20*(b) reveals significantly different field emission behavior between copper and iron based FEAs. Relatively low emission current and high turn-on fields were observed from copper-grown FEAs can be attributed to

electrostatic screening effect[22]. The tight nanorod packing resulted poor penetration of electric field between individual nanorods, thus diminishing the enhancement of electric field at the emitter apexes. A study modeling CNT field emission performance suggests that nanotube spacing approximately equal to twice their height optimizes emission performance[22]. Neither cooper nor iron-grown FEAs, *Figure 13*, in this study fulfill this criterion. Therefore, better control of nanorod areal density and alignment along with the anticipated improvement of the field emission behavior should be addressed.

Field Emission Performance Before & After Current Conditioning				
	Iron: Before Conditioning	Iron: After Conditioning	Copper: Before Conditioning	Copper: After Conditioning
$E_{threshold}$ (V/μm)	8.1	7.0	9.0	6.2
$E_{turn\text{-}on}$ (V/μm)	14.8	11.3	N/A	13.5
β_{avg}	572	676	853	1010

Table 2: Threshold, turn-on and field enhancement factor (β) for iron-grown and copper-grown ZnO nanorods before and after current conditioning.

Current conditioning has been reported for ZnO nanostructures as names like field annealing or electrical annealing[61,62]. Overall, CC improves the stability and reproducibility of the *J-E* plots through two dominant mechanisms. First, the high emission current resistively heats the emitters[48], causing desorption of surface impurities and improvments to emitter crystallinity. Secondly, CC causes smoothing of sub-micron surface impurities by ion bombardment[12], as explained in section 2.2.4.

Removal of the surface impurities found in the Auger spectra in *Figure 18*, by CC induced heating, is likely a major improvement factor of these emitters in addition to improved electrical conduction. Heating ZnO within vacuum generates oxygen vacancies

on the emitter surface, leaving unpaired electrons available for electrical conduction[30]. In a related report, ZnO had an increase in carrier concentration and reduce resistivity of thin film samples by two orders of magnitude by thermal annealing in vacuum[63, 64].

4.6 Degradation Mechanisms

4.6.1 Introduction

As previously discussed, field emission degradation mechanisms are sensitive to emitter material and morphology. Most existing literature regarding ZnO field emitters is specific to a cylindrical morphology, some with contradiction and others lacking theoretical analysis. Therefore we systematically investigated two degradation mechanisms with respect to tapered ZnO nanorods. Firstly, degradation as a result of exposure to gaseous species during field emission, and secondly, degradation resulting from high current field emission.

For experimental simplicity, field emitters synthesized on the iron substrate were used in these studies because of practically identical morphologies superior FE performance compared to Cu-grown ZnO.

4.6.2 Effects of Gas Exposure

Gaseous species are known to affect electrical properties of semiconductors which, in turn, affects field emission properties. *Figure 22* illustrates the effect gas species (H_2, N_2, and O_2 respectively) have on the field emission properties of tapered ZnO nanorods. Each graph has three *J-E* plots including scans before and after gas

exposure and a plot taken after a thermal annealing at 450°C for 30min. Thermal annealing desorbs surface bound species without ion bombardment, unlike CC.

From *Figure 22* it's clear that field emission performance had degraded as a result of exposure to each of the three gas species. Resulting from exposure to nitrogen, the maximum field emission current decreased to ~ 45% of its initial value. This comes as no surprise since nitrogen ambient has been known to decrease carrier concentration within ZnO thin films[65, 66] and has been known to degrade the FE performance of cylindrical ZnO nanorods[67]. Emission current was mostly recovered following thermal annealing.

Hydrogen exposure reduced emission current to ~55% of its initial value. However, vacuum annealing of the nanorods recovered, and even improved initial emission characteristics, with a maximum current exceeding the initial maximum. FE enhancement as a result of hydrogen has been also been reported elsewhere[20, 68] Exposure to both H and N reveals similar degradation trends. The recovery of field emission current after vacuum annealing for both H and N suggests that nanorods did not undergo any morphology degradation that might lead to a permanent alteration of emission characteristics. Therefore, it's likely that the mechanism responsible for current degradation is reversible adsorption and desorption of hydrogen and nitrogen on the emitter surface. It's worth pointing out that, the order of magnitude difference in current density between gas effect samples arises from variations induced by different synthesis batches. This doesn't detract from the scope of degradation studies.

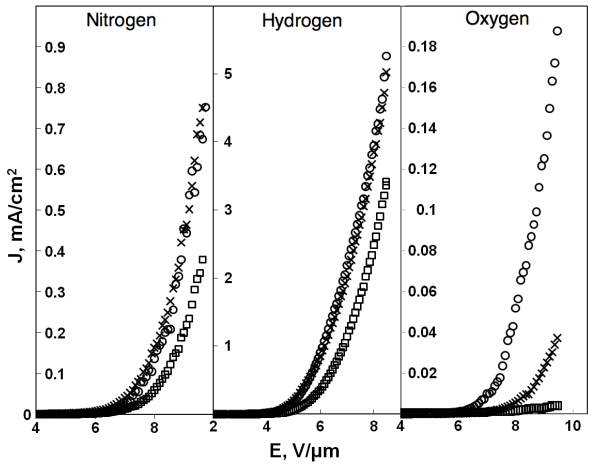

Figure 22: *The current density vs. electric field characteristics of ZnO nanorods: (symbol: ○) before gas exposure, (symbol: □) after exposure, and (symbol: ×) post vacuum-annealing at 450°C for 30 minutes relating from exposure to: (a) H_2, (b) N_2, (c) O_2. (Note: the plot corresponding to O_2 (□) is amplified 10X (y-axis) for display purposes.)*

Oxygen's negative effect on the field emission performance was most pronounced, with a final emission current being ~2% of the initial value. Vacuum annealing recovered only ~20% of the initial current. SEM analysis after the oxygen exposure has shown no observable morphology changes. This suggests that the current degradation was due to a change in the electronic structure of the nanorods' surface, likely due to filling of oxygen vacancies which is known to dominate the surface electronic properties of metal-oxides, such as ZnO[69]. Oxygen is known to decrease carrier concentration within ZnO thin-films[65,66] and degrade ZnO FE properties[67,70]. Contradictory evidence from one report suggests oxygen may improve FE characteristics by improved crystallinity, lower work function and increased conductivity[71]. To clarify this contradiction, density functional theory has been utilized in the following section.

4.6.3 Density Functional Theory Calculations

To better understand FE degradation resulting from exposure to N_2, H_2, and O_2, first-principle density functional theory (DFT) calculations are used to study variations to ZnO's electronic structure. A schematic diagram of ZnO (0001) surface geometry is shown in *Figure 23*(a). Three common adsorption sites on the Zn-(0001) surface were examined for adsorption of O_2, N_2 and H_2 gas species, including the "top", "bridge" and "hollow" sites, as depicted in *Figure 23*(a). Site (1) corresponds to the top-site, (2) is the hollow site and (3) is the bridge site. From DFT calculations, it's found that the most energetically favorable adsorption site for H was found to be on the top-site, while O and N atoms both adsorb on the hollow-site.

Change in ZnO's electronic structure was analyzed by the charge transfer and distribution when O_2, N_2 or H_2 is adsorbed on the surface. "Difference charge density" (DCD) represents the difference between charge density of the electronic ground state of non-interacting atoms with the same geometry. Projection of the DCD onto the (110) plane of the surface slab is shown in *Figure 23*(b). Adsorbates show positive charge density difference on adsorbates and surface Zn atoms show negative transfer values of charge density toward the adsorbed O_2, N_2 or H_2 molecules. This transfer of charge is consistent with the difference in the Pauling electronegativities of elements[53] (O (3.44) > N (3.04)> H (2.20)> Zn(1.65)) and is expected to induce changes in current carrier density.

The DFT calculated value for the work function of a bare ZnO surface is 5.07eV, which is close to the 5.2eV value measured at the tips of ZnO nanobelts[72]. The calculated work functions due to adsorption of H, N and O are 6.84, 6.95 and 7.12eV, respectively. *Figure 23*(c) shows the results of the total and localized density of states (DoS) for adsorbates of majority and minority spin. The localized DoS is computed by projecting the electronic density as spheres around the atoms for '*s*' state of hydrogen and '*p*' states of nitrogen and oxygen. The radii of the spheres were chosen as 1.25 Å, 0.73 Å, 0.75 Å and 0.35 Å for zinc, oxygen, nitrogen and hydrogen respectively. The position of the Fermi level is set to zero and outlined by the vertical dashed lines. As indicated in *Figure 23*(c), the shift in Fermi level for all considered adsorbates is toward the occupied electronic states. The amount of shift is largest for O_2 followed by N_2 and then H_2.

Generally, both the Fermi level shift and the available DoS near the Fermi level determine the field emission current. Based on the calculations shown in *Figure 23*(c), we expect that the field emission current would decrease in the presence of these adsorbates because the Fermi level shifts toward the valence band (increase of the work function). In other words, an additional electric field has to be applied to extract the same intensity of emission current in presence of any of the adsorbates. As evident from the projected DoS plots, oxygen, nitrogen and hydrogen have finite contribution of available states at the Fermi level and thus pronounced changes in emission current are expected. Additionally, recalling Equation 10, as work function of an emitter increases, current density decreases. These results agree well with experimental observations reported in this study.

The non-recoverable emission degradation observed in this study upon adsorption of oxygen indicates that oxygen atoms are strongly bound to the surface of nanorods. Using first principle calculations, it has been reported that adsorbed oxygen atoms on ZnO(1000) surface can fill surface vacancies and thus recover the electronic property change induced by oxygen vacancies[73]. Overall, the study indicating that oxygen improves FE characteristics of ZnO[34], resulting from decreased work function and increased conductivity, may be incorrect.

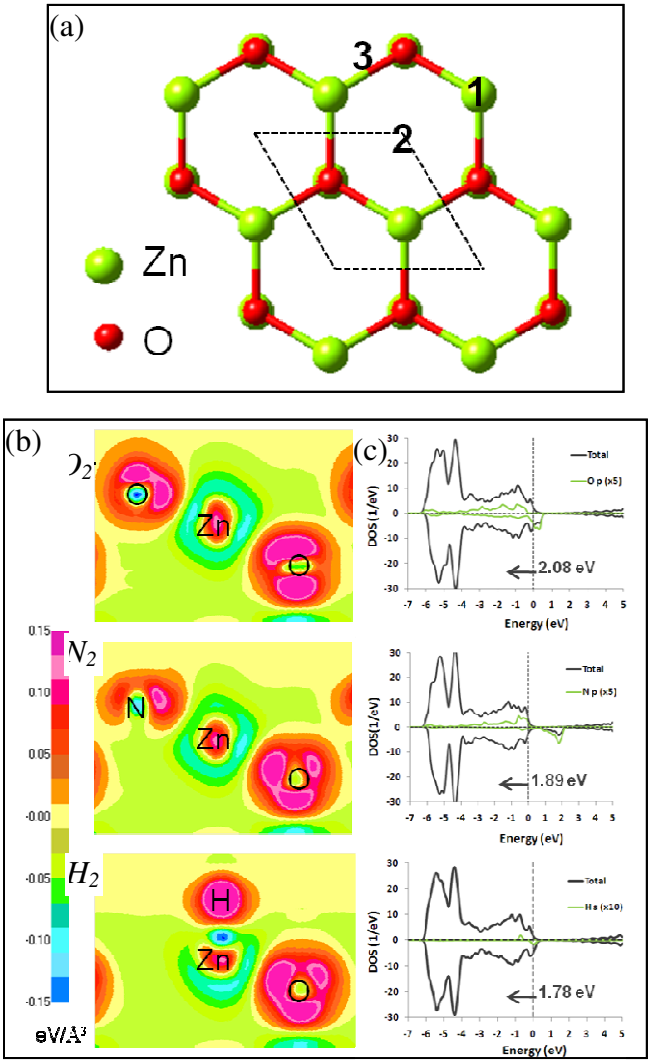

Figure 23: *(a) Schematic top-view of a polar (0001) Zn-terminated surface of a ZnO single crystal. The dashed lines show the (1x1) unit cell with lattice parameter a = 3.28Å. Numbers 1, 2, and 3 indicate the top, hollow and bridge adsorption sites respectively. (b) Difference charge density projection plot of a (110) plane where positive and negative values represent increase of charge and charge deficiency, respectively. Atoms are marked by their chemical symbols. (c) Electronic density of states (DOS) and localized projections on H s-level and O and N p-levels. Position of Fermi level is represented by vertical dashed line. The magnitude and direction of the Fermi level shift induced by the adsorbates are also marked.*

4.6.4 Effects of High Current

Extraction of high current from tapered ZnO emitters can degrade field emission performance. These changes are depicted in *Figure 24* where four successive current vs. voltage (*I-V*) plots were extracted from nanorods synthesized on a tungsten wire. *I-V* curves were used instead of *J-E* curves because the emitting area is unknown. Therefore the variable, $V_{0.1\mu A}$ will be defined as the voltage required to produce a current of 0.1μA, and will be used as a substitute for turn-on electric field (J = 0.1μA/cm^2). Additionally, "I_{250V}" will be defined as the extracted emission current at 250V.

First, an initial-scan generated baseline data for comparison (*Table 3*) reveals typical exponential *I-V* behavior (not shown in *Figure 24*) with $V_{0.1\mu A}$ = 190V and I_{250V} = 1.99μA. The subsequent scan, called "first scan" in *Figure 24*(a), has a $V_{0.1\mu A}$ that's 15V higher, increasing from 190V to 205V, with I_{250V} < 1.8μA, indicating 250V was enough to damage the emitters.

The following "second scan" shows FE current characteristics were further degraded. *Figure 24*(a) reveals that $V_{0.1\mu A}$ increased to 210V, and I_{250V} decreased to 0.5μA. The "third scan" shows an even greater increase in the $V_{0.1\mu A}$ by another 15V, going from 210V to 225V, with I_{250V} < 0.3μA. This data is presented in *Table 3*.

In order to explain the increase in $V_{0.1\mu A}$ and decrease in current in *Figure 24*(a), the sample was imaged before and after field emission scans, as shown in *Figure 24*(b) and *Figure 24*(c) respectively. Before FE scans, the nanorods had well defined sharp tips pointing radially outward, whereas, after the successive voltage scans, the nanorods

closest to the anode have blunted tips, possibly as a result of melting brought on by joule heating and/or deformation from ion bombardment.

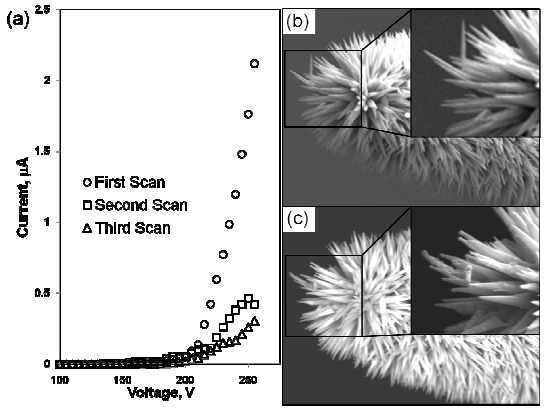

Figure 24: *(a): Field emission current vs. voltage (I-V) characteristics from ZnO nanorods synthesized on the tip of a tungsten wire after three successive high current I-V scans, resulting in high current per nanorod. Note: (I-V) data points >250V are not plotted here (b): SEM image of nanorods before high-current field emission and (c): SEM image after three high I-V scans.*

Effect of High Current ZnO Field Emission Performance				
	Test Scan (after 250V max)	1st Scan (after 250V max)	2nd Scan (after 300V max)	3rd Scan (after 350V max)
$V_{0.1\mu A}$	190	205	210	225
I_{250V} (μA)	1.99	1.76	0.47	0.26

Table 3: *Data from the successive high-current studies. Each subsequent scan indicates degradation to the emitter by increased $V_{0.1\mu A}$ and decreased I_{250V}.*

To support the possibility of tip-melting in *Figure 24*(b) & (c) a mathematical relationship specific to tapered emitters, developed by Dolan *et al.*[48], was employed. The equation is used to estimate the maximum temperature (T_{max}) at the emitter tip. Since the experimental current was drawn for relatively long times (>10 μsec), steady-state temperatures at the apex of nanorods can be assumed. Variations to physical constants of ZnO as a function temperature are not considered in the estimation. As a result, the

maximum steady-state temperature for a tapered emitter, which occurs at the nanorod apex, can be expressed by the following[48]:

$$T_{\max} = \frac{I^2 \rho \tan^2(\theta_0)}{4\pi^2 r^2 (4.18\kappa)\left(1-\cos(\theta_0)\right)^2}$$

Equation 11

Where I is the emission current per nanorod in amperes, r is the radius of the emitter tip apex in cm, ρ is the electrical resistivity in (Ω-cm), κ is the thermal conductivity in ($^{W}/_{cm\ K}$), and θ_0 is the half-angle of the emitter.

A major difficulty in estimating T_{max} is finding reliable values for the physical constants for nanoscale ZnO. For resistivity, which varies considerably with temperature, defects and size, an experimentally measured value of *98.0* Ω-cm for nanowires is chosen and a value of thermal conductivity at room temperature of *0.887W/cm* is utilized[74, 75]. Nanorod dimensions were based on the TEM image in *Figure 25* having a cone with half-angle of 2.85°, and a tip radius 4.3nm and 15μm length. Although many nanorods were present on the tip of the tungsten wire, *fFigure 24*, field emission currents were drawn from a few nanorods closest to the anode, as a result of the screening effect. If a current of 620nA is assumed for a single nanorod, which is not unreasonable for a single field emitter, an estimation from Equation 10 indicates temperature at the apex could reach 2000K. This temperature is slightly above the ZnO melting point of 1975K, and within the expected range for heat induced failure in field emission experiments[76].

Although there have been reports of melted tips on tapered field emitters of silicon[77], to the best of our knowledge, there have been no reports relating a mathematical relationship to experimental melting of a ZnO emitter tip.

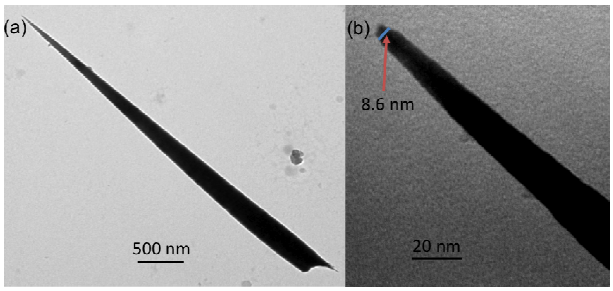

Figure 25: *TEM image of a typical ZnO nanorod taken from an iron substrate. (a) low-magnification view of an individual ZnO nanorod, (b) magnified view of the tip region of the same nanorod. Geometry constants used in T_{max} calculations were taken from this nanorod.*

In comparison to nanotubes and cylindrical-nanorods, the apex of a tapered nanorod has the smallest cross-sectional area and therefore the highest electrical resistance and current density which causes high temperatures when compared to the nanorod body. In fact, a comparison of temperature gradients for cylindrical and tapered emitters in the steady state solution showed temperature in the latter case decreases to one-half of its maximum within a distance of ten emitter radii from the apex, the same temperature change is reached for the cylindrical emitters at a distance of several thousand radii from the tip[48]. In contrast to metal emitters with roughly linearly increasing resistance with temperature, and thus has a positive feedback on heating, the resistance of ZnO decreases with temperature[78], thus has a negative impact on heating.

It is worth mentioning that, in the present study, no failure has been observed at the nanorod-substrate interface, which suggests low contact resistance.

CHAPTER 5: CONCLUSIONS AND FUTURE STUDIES

5.1 Conclusions

In summary, tapered ZnO nanorods were grown directly from copper and iron electrode substrates without seeding, using a solution processing technique. Copper surfaces promoted nucleation to a greater extent than iron, yielding higher areal density of nanorods. Field emission performance of copper-grown nanorod arrays was less than that of iron-grown arrays due to the electrostatic screening effect. Current conditioning of nanorods in high vacuum was found to significantly improve their emission characteristics as a result of desorption surface bound species like carbon and nitrogen and the generation of oxygen vacancies on the ZnO surface.

Adsorption of oxygen, nitrogen, or hydrogen onto the ZnO surface leads to an instantaneous decrease of the emission current resulting from an increase of work function, as confirmed with density functional theory calculations. Thermal annealing following gas exposure recovers lost field emission performance resulting from nitrogen and hydrogen while yielding minimal recovery for emitters exposed to oxygen.

High emission currents result in the generation of temperatures above the melting point of ZnO at the nanorod tip apex. This has been shown to physically alter the tip and degrade the emission characteristics.

5.2 Future Directions

Looking ahead, ZnO nanorods synthesized by the method in this study don't seem to be of high enough quality for use as high quality field emission sources. First, there remains inconsistency between the tip radii from one emission array to another. Finding the cause is certainly is worth tackling in the future within the context of ZnO nanorod field emitter manufacturing. Additionally, the origins of nucleation within the iron and copper substrates should be thoroughly investigated, which would help reveal some new insights of seedless ZnO nanorod growth. By doing this, it may help tune the areal density and uniformity of nanorods to match the optimal spacing of 2X the height of the nanorods. Additionally, fine-tuning of the synthesis solution is needed to fabricate well-aligned nanorods. Solving these issues would help increase the FE performance and consistency of nanorods synthesized in this manner.

It would be beneficial to identify the carbon species found on as-grown emitter surfaces and perform a DFT calculation to theoretically explain the electronic surface interactions on the (0001) ZnO tip surface. Field emission experiments in this study suggest a poor FE performance before current conditioning is partly due to the surface bound species, which a theoretical study would help to prove. For additional proof, Auger analysis of surface bound species before and after current conditioning would be a benefit. If the surface impurities are eliminated, it's rather conclusive that surface species limit the initial field emission performance before current conditioning.

Lastly, a study of the self-limiting effects of high current field emission will prove constructive. It would be interesting to note the effect of subjecting field emitters to a single maximum voltage a repeatedly, rather than using increasingly higher voltage for each scan, as had been done in this work. It would expose any self-limiting degradation as a result of tip blunting, as would be suggested by the T_{max} calculation of Equation 10

References

1. Robert Gomer, Field Emission and Field Ionization, (American Institute of Physics, New York, 1993), Chap. 1, pp. 1.

2. C. J. Edgcombe and U. Valdre, J. Microsc. 203, 188 (2001).

3. E. W. Muller, Z. Phys. A-Hadron Nucl. 106, 541 (1937).

4. R. Gomer, J. Chem. Phys. 29, 441 (1958).

5. R. Gomer, J. Chem. Phys. 63, 468 (1959).

6. W. B. Choi, D. S. Chung, J. H. Kang, H. Y. Kim, Y. W. Jin, I. T. Han, Y. H. Lee, J. E. Jung, N. S. Lee, G. S. Park and J. M. Kim, Appl. Phys. Lett. 75, 3129 (1999).

7. R. W. Wood, Phys. Rev. 5, 1 (1897).

8. O. R. Jenkins, Rep. Prog. Phys. 9, 177 (1942).

9. J. E. Lilisnfeld, Phys. Z. 23, 506 (1922).

10. K. T. Compton and I. Langmuir, Rev. Mod. Phys. 2, (no. 2) (1930).

11. W. Schottky, Z. Phys. 14, 80 (1923).

12. R. A. Millikan, and C. F. Eyring, Phys. Rev. 27, 51 (1926).

13. B. S. Gossling, Phil. Mag. 1, 609 (1926).

14. R. A. Millikan and C. C. Lauritsen, Proc. Nat. Acad. Sci. USA 14, 45 (1928).

15. C. del Rosario, J. Franklin Inst. 103, 205 (1928).

16. R. J. Piersol, Phys. Rev. 31, 441 (1928).

17. N. A. de Bruyne, Proc. Camb. Phil. Soc. 24, 518 (1928).

18. O. W. Richardson, Proc. R. Soc. A. 117, 719 (1928).

19. W. V. Houston, Z. Phys. A-Hadron Nucl. 47, 37 (1928).

20. R. H. Fowler and L. Nordheim, Proc. R. Soc. A. 119, 173 (1928).

21. L. Nordheim, Z. Phys. A-Hadron Nucl. 46, 855 (1928).

22. L. Nilsson, O. Groening, C. Emmenegger, O. Kuettel, E. Schaller, L. Schlapbach, H. Kind, J. M. Bonard and K. Kern, Appl. Phys. Lett. 76, (2000).

23. T. E. Stern, B. S. Gossling and R. H. Fowler, Proc. R. Soc. A. 124, 699 (1929).

24. V. Filip, D. Nicolaescu, M. Tanemura and F. Okuyama, Ultramicroscopy 89, 39 (2001).

25. G. S. Bocharov and A. V. Eletskii, Tech. Phys. 50, 944 (2005).

26. R. E. Hummel, Electronic Properties of Materials, 3rd edn. (Springer, New York, 2000), p. 438.

27. E. Lassner and W. D. Schubert, Tungsten - Properties, Chemistry, Technology of the Element, Alloys, and Chemical Compounds, (Springer, New York, 1999), p. 289.

28. C. A. Spindt, I. Brodie, L. Humphrey and E. R. Westerberg, J. Appl. Phys. 47, 5248 (1976).

29. E. W. Washburn, International Critical Tables of Numberical Data, Physics, Chemistry and Technology, (Knovel, 2003), p. 51-59.

30. M. H. Sukkar and H. L. Tuller, Adv. Ceramics 7, 71 (1984).

31. J. H. Edgar, S. Strite, I. Akasaki, H. Amano and C. Wetzel, Properties, Processing and Applications of Gallium Nitride and Related Semiconductors, (INSPEC/IEEE, 1999), p. 98-102.

32. M. W. Geis, J. C. Twichell, J. Macaulay and K. Okano, Appl. Phys. Lett. 67, 1328 (1995).

33. M. H. Nazare and A. J. Neves, Properties, Growth and Applications of Diamond, (INSPEC, London, 2001), p. 75-81.

34. W. Zhu, G. P. Kochanski and S. Jin, Science 282, 1471 (1998).

35. R. D. Underwood, D. Kapolnek, B. P. Keller, S. Keller, S. P. Denbaars and U. K. Mishra, Solid-State Electron. 41, 243 (1997).

36. R. H. Baughman, A. A. Zakhidov and W. A. de Heer, Science 297, 787 (2002).

37. S. T. Purcell, P. Vincent, C. Journet and V. T. Binh, Phys. Rev. Lett. 88, 105502 (2002).

38. S. C. Lim, L. C. Choi, H. J. Jeong, Y. M. Shin, K. H. An, D. J. Bae Y. H. Lee, N. S. Lee and J. M. Kim, Adv. Mater. 13, 1563 (2001).

39. Z. F. Ren, Z. P. Huang, J. W. Xu, J. H. Wang, P. Bush, M. P. Siegal and P. N. Provencio, Science 282, 1105 (1998).

40. A. Dehne and J. Mirecki, 2010, http://www.mse.engin.umich.edu/research/highlights/electrochemical-etching-of-ultrasharp-tungsten-stm-tips, 1, (2005).

41. D. M. Mattox, Handbook of Physical Vapor Deposition (PVD) Processing, (William Andrew Publishing, 1998), p. 31,35.

42. Robert H. Crabtree and D. M. Mingos, Comprehensive Organometallic Chemistry III, (Elsevier, New York, 2006), p. 47.

43. S. Kalpakjian and S. R. Schmid, in Manufacturing Processes for Engineering Materials, (Prentice Hall, Upper Saddle River, NJ, 2003), p. 766.

44. J. M. Kontio, J. Simonen, J. Tommila and M. Pessa, Microelectron. Eng. 87, 1711 (2010).

45. K. Higa and T. Asano, Jpn. J. of Appl. Phys. 43, 2749 (2004).

46. K. A. Dean, T. P. Burgin and B. R. Chalamala, Appl. Phys. Lett. 79, 1873 (2001).

47. W. Wei, Y. Liu, Y. Wei, K. Jiang, L. M. Peng, and S. Fan, Nano Lett. 7, 64 (2007).

48. W. W. Dolan, W. P. Dyke and J. K. Trolan, Phys. Rev. 91, 1054 (1953).

49. I. Brodie and C. A. Spindt, in Advances in Electronics and Electron Physics, (Academic Press, 1992), Vol. Volume 83, pp. 1-106.

50. S. Seal and S. Shukla, JOM J. Minerals, Metals and Materials Society 54, 35 (2002).

51. P. Hohenberg and W. Kohn, Phys. Rev. 136, B864 (1964).

52. W. Kohn and L. J. Sham, Phys.Rev. 140, A1133 (1965).

53. L. Pauling, The Nature of Chemical Bond, 3rd edn. (Cornell University Press, New York, 1960),

54. G. Kresse and J. Hafner, Phys. Rev.B 47, 558 (1993).

55. G. Kresse and J. Furthmuller, Phys. Rev.B 54, 11169 (1996).

56. G. Kresse and D. Joubert, Phys. Rev.B 59, 1758 (1999).

57. H. J. Monkhorst and J. D. Pack, Phys. Rev.B 13, 5188 (1976).

58. T. Sounart, J. Liu, J. Voigt, J. Hsu, E. Spoerke, Z. Tian and Y. Jiang, Adv. Func. Mater. 16, 335 (2006).

59. Y. J. Lee, T. L. Sounart, J. Liu, E. D. Spoerke, B. B. McKenzie, J. W. P. Hsu and J. A. Voigt, Cryst. Growth Des. 8, 2036 (2008).

60. M. Yang, G. Yin, Z. Huang, X. Liao, Y. Kang and Y. Yao, Appl. Surf. Sci. 254, 2917 (2008).

61. C. J. Lee, T. J. Lee, S. C. Lyu, Y. Zhang, H. Ruh and H. J. Lee, Appl. Phys. Lett. 81, 3648 (2002).

62. C. X. Xu and X. W. Suna, Appl. Phys. Lett. 83, 3806 (2003).

63. S. Major, A. Banerjee and K. L. Chopra, Thin Solid Films 122, 31 (1984).

64. J. H. Lee, B. W. Yeo and B. O. Park, Thin Solid Films 457, 333 (2004).

65. O. Hamad, G. Braunstein, H. Patil and N. Dhere, Thin Solid Films 489, 303 (2005).

66. B. D. Ahn, S. H. Oh, C. H. Lee, G. H. Kim, H. J. Kim and S. Y. Lee, J. Cryst. Growth 309, 128 (2007).

67. D. H. Kim, H. S. Jang, S. Y. Lee and H. R. Lee, Nanotechnol. 15, 1433 (2004).

68. S. H. Jo, J. Y. Lao, Z. F. Ren, R. A. Farrer, T. Baldacchini and J. T. Fourkas, Appl. Phys. Lett. 83, 4821 (2003).

69. V. E. Henrich and P. A. Cox, The Surface Science of Metal Oxides, (Cambridge University Press, UK, 1994)

70. K. S. Yeong, K. H. Maung, and J. T. L. Thong, Nanotechnol. 18, 185608 (2007).

71. Q. Zhao, X. Y. Xu, X. F. Song, X. Z. Zhang, D. P. Yu, C. P. Li and L. Guo, Appl. Phys. Lett. 88, 033102 (2006).

72. X. Bai, E. Ge Wang, P.X. Gao and Z. Lin Wang, Nano Lett. 3, 1147 (2003).

73. Y. Yan, M. M. Al-Jassim and S. H. Wei, Phys. Rev. B 72, 161307 (2005).

74. D. H. Weber, A. Beyer, B. Volkel, A. Golzhauser, E. Schlenker, A. Bakin and A. Waag, Appl. Phys. Lett. 91, 253126 (2007).

75. M. W. Wolf and J. J. Martin, Phys. Status Solidi A, 17, 215 (1973).

76. J. A. Van Vechten, Phys. Rev. B 7, 1479 (1973).

77. K. Higa and T. Asano, Jpn. J. Appl. Phys. 43, 2749 (2004).

78. M. C., Y. Caglar, S. Aksoy and S. Ilican, Appl. Surf. Sci. 256, 4966 (2010).